

exhibiting  $\delta^{34}\text{S}_{\text{sulfate-sulfide}} > 47\%$  over geologic history (2) thus might simply be related to the lack of preservation of deep-sea sediments. Euxinic basins also exhibit a wide range of  $\delta^{34}\text{S}_{\text{sulfate-sulfide}}$  values that commonly exceed 47‰ and  $^{33}\lambda$  values larger than those previously attributed to MSR (Fig. 2A). These  $\delta^{34}\text{S}_{\text{sulfate-sulfide}}$  and  $^{33}\lambda$  values have been used as an indication of the contribution of MSD to the cycling of sulfur in modern euxinic environments (27). However, the combined isotopic signatures of  $^{34}\epsilon$  and  $^{33}\lambda$  produced by DMSS-1 can explain nearly all observations from modern euxinic settings (Fig. 2A) and demonstrate that neither  $^{34}\epsilon$  nor  $^{33}\lambda$  unambiguously indicates MSD in modern environments.

The earliest values of  $\delta^{34}\text{S}_{\text{sulfate-sulfide}}$  larger than 50‰ occur in a 1.2-billion-year-old non-marine environment (13) and may have become more widespread in marine environments after ~700 million years ago (28) or even later (10, 12). Given the assumption that  $^{34}\epsilon$  values larger than 47‰ do not occur during MSR alone, this temporal trend was attributed to various mechanisms including the growth of the marine sulfate reservoir (29), the increasing importance of disproportionation (11), the progressive oxygenation of the oceans (2), and the advent of bioturbating organisms close to the Precambrian/Cambrian boundary (30). However, given that DMSS-1 in the presence of just 2 mM sulfate produces  $^{34}\epsilon$  values of 61.1‰ (Table 1) [i.e., outside the limit previously attributed to MSR alone (2, 11)], MSR alone could have produced similar S isotope signatures after a moderate increase in the size of marine sulfate reservoir (2 mM) during the mid-Mesoproterozoic (31).

In addition to  $^{34}\text{S}$  (2), the  $^{33}\text{S}$  record has been used to show the substantial contribution of MSD to the global sulfur cycle as early as 1300 million years ago (11, 32). This constraint is based on model estimates for sulfur isotope compositions ( $\delta^{34}\text{S}$  and  $\Delta^{33}\text{S}$ ) of proxies for seawater sulfate (Fig. 2B). However, the input parameters for this model include the relatively small ranges of  $^{34}\epsilon$  and  $^{33}\lambda$  values from previous laboratory experiments (11). When the same box model is solved with new expanded ranges of  $^{34}\epsilon$  and  $^{33}\lambda$  values produced by DMSS-1, all but one sample of Phanerozoic and Proterozoic sedimentary sulfates (11, 32) are consistent with the global sulfur cycle including only MSR without MSD (Fig. 2B). Therefore,  $^{33}\text{S}$  isotope signatures in sedimentary records do not clearly indicate sulfur disproportionation in the ancient oceans (2, 9, 11).

Because the fractionation of sulfur isotopes between sulfate and sulfide can exceed 50‰, even if sulfide is not reoxidized outside of the cell and at an environmental scale, more Proterozoic samples exhibiting a large  $\delta^{34}\text{S}_{\text{sulfate-sulfide}}$  value may be found. Any temporal changes in the sulfur isotope record during this time could reflect the changing nature of organic material that fueled sulfate reduction, rather than measure the extent of oxygenated areas in oceans. The relative contributions of MSR alone and of the environmental-

scale oxidative recycling toward large present and past natural fractionations of S isotope ratios now remain to be evaluated.

## References and Notes

- R. M. Garrels, A. Lerman, *Proc. Natl. Acad. Sci. U.S.A.* **78**, 4652 (1981).
- D. E. Canfield, A. Teske, *Nature* **382**, 127 (1996).
- R. A. Berner, S. T. Petsch, *Science* **282**, 1426 (1998).
- $\delta^{34}\text{S}_{\text{sulfate-sulfide}}$  is the depletion of  $^{34}\text{S}$  in sulfide relative to sulfate source (e.g., seawater sulfate for marine environments) ( $\approx \delta^{34}\text{S}_{\text{sulfate}} - \delta^{34}\text{S}_{\text{sulfide}}$ ).  $\delta^x\text{S}$  values are defined as  $\delta^x\text{S} = 1000 \cdot [(^{x}\text{S}/^{32}\text{S})_{\text{sample}} / (^{x}\text{S}/^{32}\text{S})_{\text{standard}} - 1]$ , where  $x$  is 33 or 34.  $\Delta^{33}\text{S} = \delta^{33}\text{S} - 1000 \cdot [(\delta^{34}\text{S}/1000 + 1)^{0.515} - 1]$ .  $^{34}\epsilon = 1000 \cdot [1 - (^{34}\text{S}/^{32}\text{S})_{\text{sulfide}} / (^{34}\text{S}/^{32}\text{S})_{\text{sulfate}}]$  and  $^{33}\lambda = \ln[(^{33}\text{S}/^{32}\text{S})_{\text{sulfide}} / (^{33}\text{S}/^{32}\text{S})_{\text{sulfate}}] / \ln[(^{34}\text{S}/^{32}\text{S})_{\text{sulfide}} / (^{34}\text{S}/^{32}\text{S})_{\text{sulfate}}]$ , where  $(^{34}\text{S}/^{32}\text{S})_{\text{sulfide}}$  and  $(^{34}\text{S}/^{32}\text{S})_{\text{sulfate}}$  are the instantaneous S isotope ratios of sulfide and the remaining sulfate, respectively.
- M. D. Rudnicki, H. Elderfield, B. Spiro, *Geochim. Cosmochim. Acta* **65**, 777 (2001).
- U. G. Wortmann, S. M. Bernasconi, M. E. Böttcher, *Geology* **29**, 647 (2001).
- B. Brunner, S. M. Bernasconi, *Geochim. Cosmochim. Acta* **69**, 4759 (2005).
- D. E. Canfield, J. Farquhar, A. L. Zerkle, *Geology* **38**, 415 (2010).
- D. E. Canfield, B. Thamdrup, *Science* **266**, 1973 (1994).
- M. T. Hurtgen, M. A. Arthur, G. P. Halverson, *Geology* **33**, 41 (2005).
- D. T. Johnston *et al.*, *Science* **310**, 1477 (2005).
- D. A. Fike, J. P. Grotzinger, L. M. Pratt, R. E. Summons, *Nature* **444**, 744 (2006).
- J. Parnell, A. J. Boyce, D. Mark, S. Bowden, S. Spinks, *Nature* **468**, 290 (2010).
- M. S. Sim, S. Ono, K. Donovan, S. P. Templer, T. Bosak, *Geochim. Cosmochim. Acta.*, published online 23 May 2011 (10.1016/j.gca.2011.05.021).
- B. J. Peterson, R. W. Howarth, R. H. Garritt, *Ecology* **67**, 865 (1986).
- Materials and methods are available as supporting material on Science Online.
- B. Vu, M. Chen, R. J. Crawford, E. P. Ivanova, *Molecules* **14**, 2535 (2009).
- J. M. Stams, M. Veenhuis, G. H. Weenk, T. A. Hansen, *Arch. Microbiol.* **136**, 54 (1983).
- K. Mopper *et al.*, *Mar. Chem.* **10**, 55 (1980).
- C. E. Rees, *Geochim. Cosmochim. Acta* **37**, 1141 (1973).
- D. B. Northrop, *Annu. Rev. Biochem.* **50**, 103 (1981).
- The range reflects values derived by either extrapolation from high temperature (>200°C) or theoretical calculations (33), assuming pH = 7. The equilibrium isotope fractionation factor between aqueous  $\text{H}_2\text{S}$  and  $\text{HS}^-$  is ~6‰.
- J. Farquhar *et al.*, *Geobiology* **1**, 27 (2003).
- B. B. Jørgensen, *Science* **249**, 152 (1990).
- S. D'Hondt, S. Rutherford, A. J. Spivack, *Science* **295**, 2067 (2002).
- B. B. Jørgensen, A. Boetius, *Nat. Rev. Microbiol.* **5**, 770 (2007).
- A. L. Zerkle *et al.*, *Geochim. Cosmochim. Acta* **74**, 4953 (2010).
- G. M. Ross, J. D. Bloch, H. R. Krouse, *Precambrian Res.* **73**, 71 (1995).
- J. M. Hayes, I. B. Lambert, H. Strauss, in *The Proterozoic Biosphere: A Multidisciplinary Study*, J. W. Schopf, C. Klein, Eds. (Cambridge Univ. Press, Cambridge, 1992), pp. 129–132.
- D. E. Canfield, J. Farquhar, *Proc. Natl. Acad. Sci. U.S.A.* **106**, 8123 (2009).
- L. C. Kah, T. W. Lyons, T. D. Frank, *Nature* **431**, 834 (2004).
- N. Wu, J. Farquhar, H. Strauss, S.-T. Kim, D. E. Canfield, *Geochim. Cosmochim. Acta* **74**, 2053 (2010).
- T. Otake, A. C. Lasaga, H. Ohmoto, *Chem. Geol.* **249**, 357 (2008).
- D. T. Johnston, J. Farquhar, D. E. Canfield, *Geochim. Cosmochim. Acta* **71**, 3929 (2007).
- X. Li *et al.*, *Geochim. Cosmochim. Acta* **74**, 6764 (2010).

**Acknowledgments:** We thank W. Olszewski, K. Donovan, S. Templer, J. Seewald, S. Sylva, B. Weiss, L. Kump, J. Grabenstatter, B. Bannan, P. Hedman, and Y. J. Joo. This work was partially supported by NASA Astrobiology Institute (#NNA08CN84A).

## Supporting Online Material

www.sciencemag.org/cgi/content/full/333/6038/74/DC1  
Materials and Methods  
SOM Text  
Fig. S1  
Tables S1 to S5  
References (36–133)

3 March 2011; accepted 16 May 2011  
10.1126/science.1205103

# Formation and Spread of Aircraft-Induced Holes in Clouds

Andrew J. Heymsfield,<sup>1\*</sup> Gregory Thompson,<sup>1</sup> Hugh Morrison,<sup>1</sup> Aaron Bansemer,<sup>1</sup> Roy M. Rasmussen,<sup>1</sup> Patrick Minnis,<sup>2</sup> Zhien Wang,<sup>3</sup> Damao Zhang<sup>3</sup>

Hole-punch and canal clouds have been observed for more than 50 years, but the mechanisms of formation, development, duration, and thus the extent of their effect have largely been ignored. The holes have been associated with inadvertent seeding of clouds with ice particles generated by aircraft, produced through spontaneous freezing of cloud droplets in air cooled as it flows around aircraft propeller tips or over jet aircraft wings. Model simulations indicate that the growth of the ice particles can induce vertical motions with a duration of 1 hour or more, a process that expands the holes and canals in clouds. Global effects are minimal, but regionally near major airports, additional precipitation can be induced.

The passage of aircraft through subfreezing, supercooled liquid water cloud can produce circular and linear voids called

hole-punch and canal clouds on the basis of their distinctive appearance (Fig. 1A).

Ice streamers embedded within or descending from circular holes or elongated channels carved out of mid-level, subfreezing cloud layers were first reported in the meteorological literature in the 1940s (1). In correspondence titled “Man-Made Cirrus?” in *Weather* (2), a large horizontal loop sketched in a midlevel cloud was the first of

<sup>1</sup>National Center for Atmospheric Research (NCAR), Boulder, CO 80301, USA. <sup>2</sup>NASA Langley Research Center, Hampton, VA 23681, USA. <sup>3</sup>Department of Atmospheric Sciences, University of Wyoming, Laramie, WY 82071, USA.

\*To whom correspondence should be addressed. E-mail: heyms1@ncar.ucar.edu

such features to be attributed to an aircraft. A photograph published two decades later in “Hole-in-Cloud: A Meteorological Whodunit?” generated considerable interest from the U.S. meteorological community as to its cause (3). In the 1980s, research aircraft studying ice formation in supercooled clouds observed that their propeller aircraft produced copious ice crystals that confounded their observations and interpretations (4, 5). Working from the premise that holes in clouds can indicate inadvertent seeding by aircraft and drawing on a series of images of holes and canals together with modeling of ice injection into a supercooled cloud, we examined aircraft-induced inadvertent seeding effects within supercooled cloud layers.

Ice nuclei such as dust are generally required to freeze supercooled droplets at temperatures above  $-40^{\circ}\text{C}$ . Supercooled droplets are not found at temperatures below this point because droplets freeze spontaneously at about  $-40^{\circ}\text{C}$ . Once produced in a supercooled cloud, ice grows rapidly at the expense of the droplets. According to the Bergeron-Findeisen (B-F) process, if ice is introduced into a supercooled cloud, the liquid droplets will be at subsaturation relative to the ice; the liquid will evaporate, condensing and freezing onto the ice crystals and causing them to grow larger. This process is the basis for cloud seeding operations that convert supercooled droplets into snow.

The passage of an aircraft through a supercooled cloud can cause cooling sufficient to initiate the formation of ice crystals at cloud temperatures of  $-10$  to  $-20^{\circ}\text{C}$  and the subsequent operation of the B-F process (4, 5). Expansion of air behind aircraft propeller tips produces 20 to  $30^{\circ}\text{C}$  of cooling, and flow of air over the wings of jet aircraft at cruise speed produces  $20^{\circ}\text{C}$  of cool-

ing, creating aerodynamic contrails in high relative humidity conditions (6, 7). In both instances, cooling can induce spontaneous droplet freezing.

The operation of the B-F process in the context of inadvertent seeding is illustrated in Fig. 1B. It shows bands of enhanced radar signal embedded in a low-level supercooled cloud layer; a local sounding showed that the layer had a minimum temperature of about  $-16^{\circ}\text{C}$ . The enhanced radar signal convert to snowfall-accumulation rates up to about  $23\text{ mm hr}^{-1}$  (8), assuming an average 12:1 snowfall-accumulation-to-liquid-precipitation rate in Colorado storms. Snowbands are generally linear, so the curved nature of these bands and their path and proximity to the runways all suggest that it is probable they were induced by aircraft.

If a supercooled cloud is vertically thin or the cloud water is not replenished, snow can develop and fall out, leaving holes and voids in clouds. On 29 January 2007, over Texas and neighboring states a sequence of 20 visible images of an extensive cloud layer with embedded holes and canals was obtained with the Geostationary Operational Environmental Satellite (GOES-12) (Fig. 2, A and B). These images spanned a 4-hour period from 1632 to 2032 UTC, at 15- or 30-min intervals, when the holes and canals were most prevalent.

The characteristics of the cloud layer were identified from local radiosondes, wind profilers, and the sequence of GOES imagery. The cloud altitude was  $\sim 7.7\text{ km}$ , and cloud top temperature was  $\sim -30^{\circ}\text{C}$  (7). From soundings, reanalyzed to correct for humidity sensor time lag indicating a relative humidity of approximately 100% with respect to water in the cloud layer, from satellite imagery indicating an approximately  $10\text{-}\mu\text{m}$  radius of the cloud particles (7) characteristic of droplet populations, and the near absence of snow

virga except in localized regions of ice fallout in photographic images taken from the ground (Fig. 3A), we conclude that this cloud layer was primarily liquid. The liquid cloud layer was approximately 150 m deep. Below it, there was a 450-m layer favorable for ice growth with relative humidities above ice saturation conditions at the ambient temperatures. The wind speed in the cloud environment is relevant to the advection speed of the holes: From radiosondes, wind profilers, and tracking of individual holes, the mean horizontal wind velocity in the cloud layer was about  $40\text{ m s}^{-1}$ .

We followed a total of 92 features from their first appearance on a satellite image until they were no longer visible or until the end of the time period had been reached (Fig. 2B). Some holes reached lengths of  $>100\text{ km}$  and were detected for 4 or more hours.

From the consecutive 15-min satellite images, we measured the hole diameters and fractional increases of the area with time (fig. S2). Over the first 30 min from detection, the holes doubled their area. From 30 to 60 min, identifiable holes increased in area by 25%. After 1 hour from first detection, the holes' areas slowly decreased.

Hole-producing aircraft were identified from Federal Aviation Administration (FAA)-archived track information (9). Candidate aircraft were selected as those that flew within the altitude range of 7 to 8 km and within close proximity in time and  $[x, y]$  positions relative to specific features (fig. S1). Not all holes could be attributed definitively to a single aircraft because of a regular succession of aircraft along certain flight corridors. In such an instance, the hole was ignored in the analysis, or if the candidate aircraft were of the same model and manufacturer, the

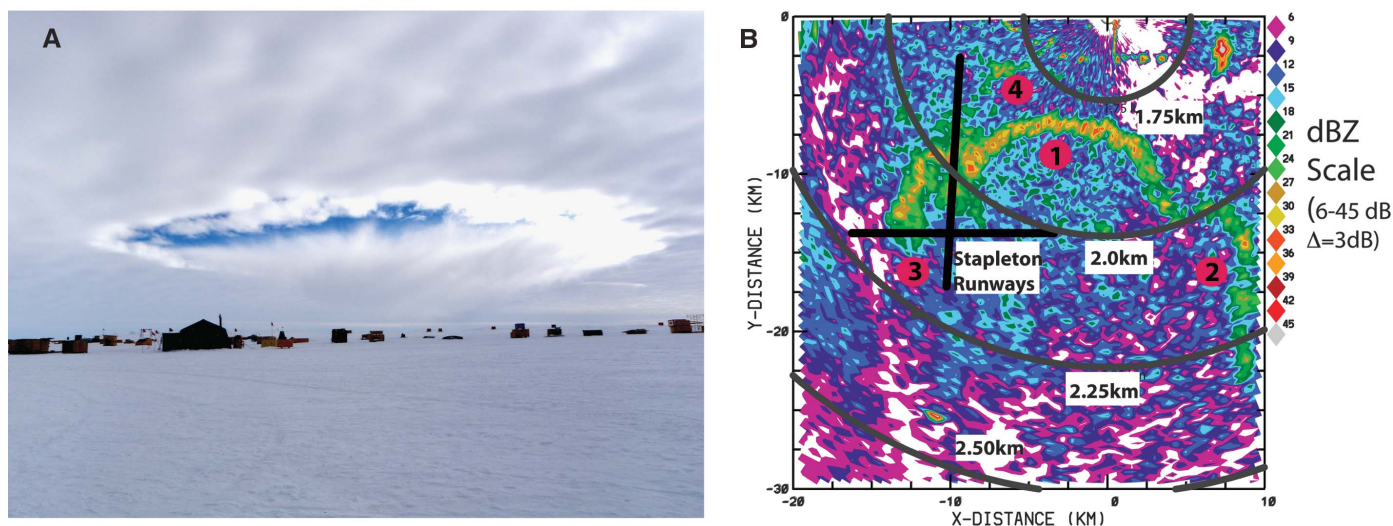


**Fig. 1.** (A) Aircraft-induced hole observed at the West Antarctic Ice Sheet Divide Camp, Antarctica ( $79^{\circ}28.058'\text{S}$   $112^{\circ}05.189'\text{W}$ , 1806 m elevation) on 12 Dec 2009, 1400 New Zealand Time. The cloud's bright cumiform structure with gray fallstreaks below are visible. The hole first appeared on the horizon and then moved toward the camera. It is likely that a LC130 aircraft produced the ice that formed the hole. [Photo provided by Eric Zrubek and Michael Carmody] (B) Radar reflectivity measurements taken

on 3 December 1992 by the NCAR Mile High Radar near the former Stapleton (Denver, Colorado) Airport. The radar antenna was operating at 1.6 degrees, so that the observed height through the cloud layer increases with distance (shown by the range rings in altitude increments of 250 m). The airport north-south and east-west runways are indicated. Arcs of snow generated by unknown aircraft (labeled 1 to 4) are observed to fall from a higher (left) to lower level.



most likely track among these similar aircraft was chosen.

Three-quarters of the hole-producing aircraft were identified. On this day, a full spectrum of aircraft types was found to produce the holes and canals: large passenger jets, regional jets, private jets, military jets, turboprop, and prop/piston (table S1).

This analysis supports the previous findings that there are at least two modes of inadvertent cloud seeding: expansion of air around aircraft propeller tips as shown observationally (4) and cooling of air over the wings of jet aircraft at cruise speeds as shown from numerical models and empirically (6, 7). Although engine combustion products are not a good source of ice nuclei, additional ice may be produced from combustion.

Because holes and canals were found to expand appreciably and persisted over extended periods, we were left with the conclusion that there must be more to their development and persistence than

solely the operation of the B-F process. The dynamical theory of cloud seeding states that the injection of ice particles into a supercooled cloud layer releases latent heat, creating buoyancy in the ice-affected region and producing or invigorating updrafts. It is plausible that a small-scale and persistent updraft could develop in the ice region with compensating downdrafts on the outside edges, causing the water cloud to erode by evaporation (7).

To support or dismiss the idea that this process plays a role in the development and maintenance of these features, simulations of inadvertent seeding of this supercooled layer were conducted by using the Weather Research and Forecasting (WRF) model (10). The WRF model was configured with 600 by 300 horizontal grid points spaced 50 m apart and 135 vertical levels spaced 150 m apart near the earth's surface, 50 m apart in the kilometer surrounding the depth of the cloud, and 250 m apart well above cloud top. Smoothly

varying vertical spacing was applied between these points. We used the Fort Worth, Texas, rawinsonde data for input thermodynamic and wind conditions. The change in wind speed of  $2 \text{ m s}^{-1}$  (corresponding to a horizontal wind shear of  $0.013 \text{ s}^{-1}$ ) was specified through the 150-m deep liquid cloud layer.

The model was initialized with an adiabatic cloud liquid water profile. The Thompson cloud scheme (11) was used; it considers processes such as evaporation of droplets and growth by vapor diffusion of ice through the B-F process, release of latent heat, fallout of ice crystals, and other related processes. Radiation and land-surface exchange with the atmosphere were neglected for simplicity. In the simulation, ice production was intentionally disabled for the first 30 simulated minutes. Then, ice crystal concentration was increased to 1000 per liter and held constant for 60 s in a 250- by 250-m region through the depth of the cloud layer so as to simulate ice production by an aircraft penetrating the liquid layer. This concentration is consistent with the concentration of ice crystals measured by research aircraft that have sampled regions of inadvertent ice production by research aircraft (7, 12). From this point forward, no additional ice crystals were introduced.

The model calculations at a snapshot in time are compared visually with a photograph from the ground in Fig. 3, A and B. The simulation exhibits the expected vapor depositional growth of ice and evaporation of water droplets, leading to a hole in the liquid layer (Fig. 3B). The slope of the bottom edge of the snow (which is displaced horizontally about 4 km over a depth of 0.6 km) is consistent with the vertical wind shear of  $0.013 \text{ s}^{-1}$  and snow fallspeed of  $0.6 \text{ m s}^{-1}$ .

More quantitative evaluations of the development of the ice and snow field and the vertical air motions are shown for a sequence of times in Fig. 4, left. For clarity, only the snow and vertical velocity fields are shown and not the ice field. Latent heating associated with vapor deposition leads to a  $15 \text{ cm s}^{-1}$  updraft near the hole center that suspends most of the ice, although some particles are converted to faster-falling snow crystals, which fall through the updraft and produce snow fallstreaks beneath the hole. Downdrafts on the periphery of the hole accelerate evaporation of liquid water, and the hole rapidly widens over time. The spreading rate of the simulated cloud hole is relatively uniform in both wind-parallel and -perpendicular directions. The hole more than doubles in diameter, from 2 to 4.4 km, between 30 and 90 min. This increase is quite similar to the spread rate of the observed holes between 30 and 90 min (fig. S2). However, a more direct comparison between model simulation and observed hole clouds is hindered because the satellite is unable to observe the initial stages of transit of the various aircraft through the supercooled cloud is not known. With no additional ice crystals nucleated, ice and snow begin to dissipate after 90 min.

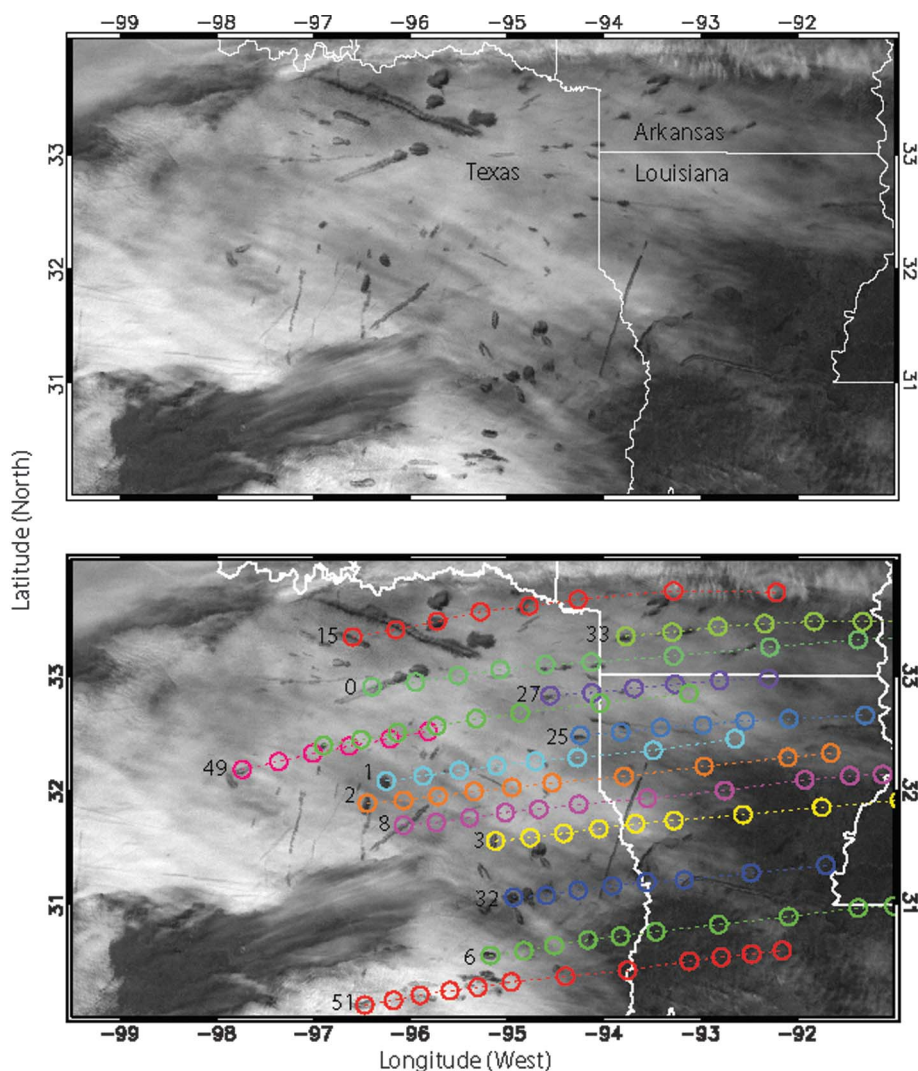
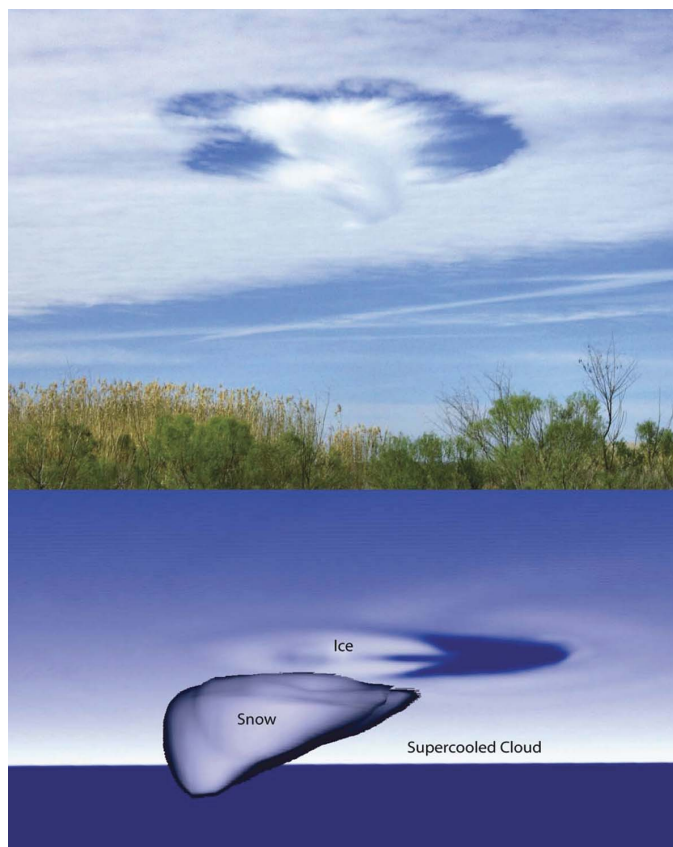


**Fig. 2.** Imagery from the GOES satellite on 29 January 2007. **(Top)** Circular and linear aircraft-induced holes at 1632 UTC, and **(bottom)** example of paths of multiple holes, with circles indicating the midpoint position of each hole or canal at 15-min intervals from first through last detection. An identifying hole number is given at the beginning time of the first detection of each hole.

**Fig. 3. (Top)** Photograph of aircraft-induced hole observed on 29 January 2007 as viewed toward the west. [Photograph courtesy of Jafvis] **(Bottom)** Simulated snow fallstreaks at 60 min after the introduction of ice into the cloud layer.



We performed two additional sensitivity tests to understand processes that lead to the hole development and growth. In the first test, latent heating due to vapor depositional growth of ice was turned off, but latent cooling from droplet evaporation was retained. Although the dynamics are weaker in this simulation and there is no clear updraft in the hole center, there are still downdrafts of several centimeters per second on the periphery of the hole driven by cooling from droplet evaporation. This leads to some growth of the hole, but at a reduced rate as compared with the baseline simulation (Fig. 4, right). In the second sensitivity test, all latent heating and cooling was turned off. As a result, the cloud dynamics are very weak, with vertical motions generally less than  $1 \text{ cm s}^{-1}$ . A hole still develops in this simulation because of ice growth at the expense of liquid water (the B-F process), but the spread of the hole is effectively eliminated. Overall, these tests indicate that interactions between microphysics and dynamics through both latent heating and evaporative cooling are the key to explaining rapid hole growth.

Because propeller and jet aircraft-induced cloud seeding and dynamical effects can ensue after the injection of inadvertent ice into a supercooled layer, potential exists in and around heavily trafficked airports for the generation of precipitation, as illustrated in Fig. 1B. Conditions suitable for inadvertent seeding of clouds were quantified for five major midlatitude and two high-latitude airports: London Heathrow; Frankfurt; Charles De Gaulle, Paris; Seattle-Tacoma; Chicago O'Hare; Yellowknife, Canada; and Byrd Station, Antarctica (13). Colocated data collected from the spaceborne Cloud-Aerosol Lidar and Infrared Pathfinder Satellite Observations (CALIPSO) lidar and CloudSat cloud radar from June 2006 to May 2008 were used to estimate how often supercooled clouds occur within a 100-km radius of selected primary airports in mid- and high latitudes (14). A commercial aircraft will cover this horizontal distance when climbing to about 10,000 feet (3 km), where many of the supercooled cloud layers are noted. Comparative frequencies of occurrence at the six airports are shown in fig. S3.

Taking temperatures of  $-10^\circ\text{C}$  and below to be conducive to ice production by propeller aircraft and below  $-20^\circ\text{C}$  for jet aircraft, the former have about a 5 or 6% probability (annual average) of inadvertently seeding clouds, whereas jets have a 2 to 3% probability for these locations. Although the ensuing dynamical effects are situational, our modeling suggests that the generation of precipitation amount and duration would be enhanced through subsequent dynamical effects. Although aircraft might seed these clouds, visible holes will not necessarily be produced if substantial ice is already present, if the cloud layers are thick, or if the dynamics are not favorable for their formation.

Hole-punch clouds induced aerodynamically by propeller and jet aircraft are a signature of a larger cloud process at work: inadvertent seeding

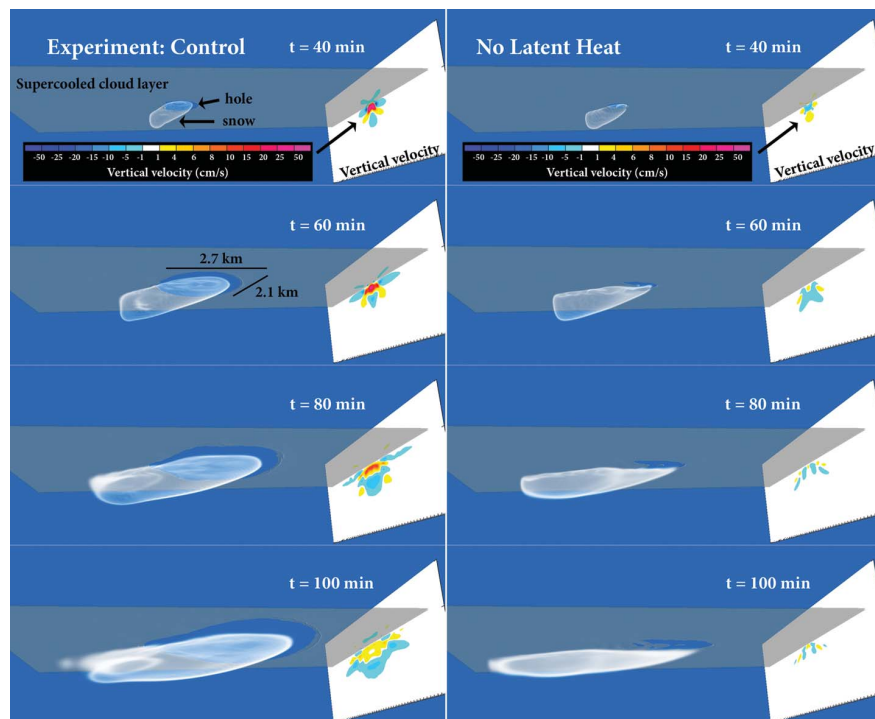


**Fig. 4.** Modeled fields of cloud (dark gray parallelogram, 14.5 km by 7.5 km, 50 m resolution), snow locations (gray shading), and a vertical slice of averaged vertical velocities (colored contours) located approximately along the wind direction. The model results are shown at 40, 60, 80, and 100 min after model initialization and 10, 30, 50, and 70 min after the introduction of ice. Color bar shows vertical velocity scale. **(Left)** Ice growth with latent heat released. **(Right)** Ice growth with latent heat turned off.



of ice in supercooled clouds at temperatures below about  $-10$  or  $-20^{\circ}\text{C}$ . It has already been established that contrails affect the atmosphere primarily at temperatures below  $-40^{\circ}\text{C}$  (15). This process extends the envelope for aircraft effects on the atmosphere to warmer temperatures. Inadvertent seeding may not be important globally, but regionally near major airports in midlatitudes during cool weather months it may lead to enhanced precipitation at the ground. Polar clouds are particularly susceptible to the effect, modifying incoming and outgoing radiative fluxes near the surface and therefore local meteorology and climatology.

#### References and Notes

1. V. C. Schumacher, *Z. Angew. Met.* **57**, 214 (1940).
2. *Weather* **3**, 232 (1948).
3. *Weatherwise* **21**, 1 (1968).
4. A. L. Rangno, P. V. Hobbs, *J. Clim. Appl. Meteorol.* **22**, 214 (1983).
5. A. L. Rangno, P. V. Hobbs, *J. Clim. Appl. Meteorol.* **23**, 985 (1984).
6. K. Gierens, B. Kärcher, H. Mannstein, B. Mayer, *J. Atmos. Sci.* **66**, 217 (2009).
7. A. J. Heymsfield *et al.*, *Bull. Am. Meteorol. Soc.* **91**, 753 (2010).
8. R. S. Sekhon, R. C. Srivastava, *J. Atmos. Sci.* **27**, 299 (1970).
9. The selection of candidate aircraft is available as supporting material on *Science* Online, together with a table detailing aircraft types and numbers.
10. W. C. Skamarock, J. B. Klemp, *J. Comput. Phys.* **227**, 3465 (2008).
11. G. Thompson, P. R. Field, R. M. Rasmussen, W. D. Hall, *Mon. Weather Rev.* **136**, 5095 (2008).
12. W. L. Woodley *et al.*, *J. Appl. Meteorol.* **42**, 640 (2003).
13. The method of quantification is available as supporting material on *Science* Online.
14. D. Zhang, Z. Wang, D. Liu, *J. Geophys. Res.* **115**, D00H13 (2010).
15. H. Appleman, *Bull. Am. Meteorol. Soc.* **34**, 14 (1953).
16. The authors wish to thank contributors to the data used in this study: N. Mirsky, N. Downs, E. Zrubek, M. Carmody, B. Skamarock, J. Tuttle, P. Kennedy, C. Velden, D. Spangenberg, and J. Robaidek. Editing by M. Miller and graphics with particular help from A. Norton, co-developer of VAPOR software, are greatly appreciated. This research was supported by the National Center for Atmospheric Research through NSF, through NASA from grants NNX07AQ85G and NNX10AN18G, and through the FAA Aviation Climate Change Research Initiative.

#### Supporting Online Material

[www.sciencemag.org/cgi/content/full/333/6038/77/DC1](http://www.sciencemag.org/cgi/content/full/333/6038/77/DC1)

Materials and Methods

Figs. S1 to S3

Table S1

13 January 2011; accepted 19 May 2011

10.1126/science.1202851

## Pattern in Escalations in Insurgent and Terrorist Activity

Neil Johnson,<sup>1</sup> Spencer Carran,<sup>2,3</sup> Joel Botner,<sup>4</sup> Kyle Fontaine,<sup>5</sup> Nathan Laxague,<sup>1</sup> Philip Nuetzel,<sup>5</sup> Jessica Turnley,<sup>6</sup> Brian Tivnan<sup>7,8</sup>

In military planning, it is important to be able to estimate not only the number of fatalities but how often attacks that result in fatalities will take place. We uncovered a simple dynamical pattern that may be used to estimate the escalation rate and timing of fatal attacks. The time difference between fatal attacks by insurgent groups within individual provinces in both Afghanistan and Iraq, and by terrorist groups operating worldwide, gives a potent indicator of the later pace of lethal activity.

In 1948, Lewis Fry Richardson found that the number of wars with a given number of fatalities follows an approximate power-law statistical distribution as a function of the number of fatalities (1). Recent research has shown that a similar statistical distribution arises for the number of fatalities in individual clashes and acts of terrorism (2, 3), whereas the relative stability of these distributions over time allows an estimate to be given of the severity of future wars or clashes within an ongoing war (2–4). However, these existing studies say nothing about the operationally relevant questions (5–7) of how the underlying arms race evolves over time, or when fatal attacks might occur. Here, we confront these questions using fatality data obtained on an unprecedented daily scale from the ongoing insurgent war in Afghanistan and the recent one in Iraq. Our data analysis is freely available for public scrutiny: The coalition military fatality data come from the public Web site [www.icasualties.org](http://www.icasualties.org). Our analysis was done with the free down-

loadable tool Open Office, which runs on any computer platform. The supporting online material (SOM) for this paper contains step-by-step instructions together with Open Office worksheets. For Afghanistan, we include fatalities from the start of Operation Enduring Freedom in 2001 until summer 2010, when General Petraeus became commander of the International Security Assistance Force and the U.S.-led surge started. For Operation Iraqi Freedom, the data include fatalities from 2003 until summer 2010, when U.S. military action officially ended. The terrorism results are derived from a recent study, which used the database of the Memorial Institute for the Prevention of Terrorism, comprising the 3143 fatal attacks carried out by the 381 known terrorist groups operating within the period 1968–2008 (8). Suicide bombing data for Hezbollah (1982–1985) and Pakistan militants (1995–2008) comes from the public Web site <http://cpost.uchicago.edu>.

For a wide range of human activities, the time taken to complete a given challenging task decreases with successive repetitions, following an approximate power-law progress curve (8–12). This inspires us to analyze the insurgents' completion of fatal attacks against coalition military forces in a similar way (Fig. 1, A and B). We calculated the best-fit power-law progress curve  $\tau_n = \tau_1 n^{-b}$ , where  $\tau_n$  represents the interval between the  $(n - 1)$ 'th and  $n$ 'th fatal day (one in which the insurgent activity produces at least one

coalition military death), where  $n = 1, 2, 3$ , etc.  $b$  indicates the escalation rate.  $\tau_1$  is the time interval between the first 2 days with coalition military fatalities. (For global terrorism, a fatal day is one in which a particular terrorist group produced at least one death anywhere in the world.) Figure 1C shows the best-fit values  $\tau_1$  and  $b$  for each province in Afghanistan, for all forms of hostile death. The average number of fatalities per fatal attack is fairly constant in a conflict (2, 3, 8), hence it is in insurgents' interest (or that of a particular terrorist group) that the time between fatal days decrease rapidly, and hence  $b$  is large and positive, while the opposite is true for the military (or counterterrorism force). The scatter in  $\tau_n$  in Fig. 1B is typical for real-world tasks (in particular, given the ongoing two-way struggle), and the Pearson rank product-moment correlation coefficient ( $R^2$ ) is within an acceptable range for social systems (9–14). Although alternative progress curve forms are possible, any such two-parameter progress curve amounts to a nonlinear transformation of the power-law form and hence generates a more complex version of Fig. 1C. An exponential form does not generate systematically better progress-curve fits;  $R^2$  for the power-law form is better by up to 70% for three-quarters of the provinces, including (most importantly) those with the most data points, and only tends to be comparable for the few provinces having sparse datapoints and larger  $\tau_n$  scatter. We do not consider events with no deaths because they occur almost daily; moreover, the injury statistics are not publicly available. Although the data resolution time scale is 1 day, this is not problematic, because the  $\tau_n$  values dictating the best-fit progress curve for a given province, or terrorist group, are usually much larger than 1.

Figure 1C reveals a surprising linear relationship between the best-fit progress curve values  $\tau_1$  and  $b$  for individual provinces. The straight line through the provinces has  $R^2 = 0.9$  and is given by the equation  $b = m \log_{10} \tau_1 + c$ , with best-fit parameter values  $m = 0.89$  and  $c = -1.22$ . Even if one speculated that the  $\tau_1$  and  $b$  values have to lie somewhere in this range (which, a priori,

<sup>1</sup>Department of Physics, University of Miami, Coral Gables, FL 33124, USA. <sup>2</sup>Department of Biology, University of Miami, Coral Gables, FL 33124, USA. <sup>3</sup>Department of Mathematics, University of Miami, Coral Gables, FL 33124, USA. <sup>4</sup>Department of Computer Science, University of Miami, Coral Gables, FL 33124, USA. <sup>5</sup>Department of International Studies, University of Miami, Coral Gables, FL 33124, USA. <sup>6</sup>Galisteo Consulting Group, Albuquerque, NM 87110, USA. <sup>7</sup>The MITRE Corporation, McLean, VA 22102, USA. <sup>8</sup>Complex Systems Center, University of Vermont, Burlington, VT 05405, USA.

## ERRATUM

*Post date 10 February 2012*

---

**Reports:** "Formation and spread of aircraft-induced holes in clouds" by A. J. Heymsfield *et al.* (1 July 2011, p. 77). The photo used in Fig. 1A was incorrectly credited. The credit should read, "Photo provided by Eric M. Brown, technical background by Michael Carmody." The credit has been corrected in the HTML version online.



## Formation and Spread of Aircraft-Induced Holes in Clouds

Andrew J. Heymsfield *et al.*

*Science* **333**, 77 (2011);

DOI: 10.1126/science.1202851

*This copy is for your personal, non-commercial use only.*

If you wish to distribute this article to others, you can order high-quality copies for your colleagues, clients, or customers by [clicking here](#).

Permission to republish or repurpose articles or portions of articles can be obtained by following the guidelines [here](#).

**The following resources related to this article are available online at [www.sciencemag.org](http://www.sciencemag.org) (this information is current as of December 6, 2015 ):**

A correction has been published for this article at:

<http://www.sciencemag.org/content/335/6069/657.1.full.html>

**Updated information and services**, including high-resolution figures, can be found in the online version of this article at:

<http://www.sciencemag.org/content/333/6038/77.full.html>

**Supporting Online Material** can be found at:

<http://www.sciencemag.org/content/suppl/2011/06/29/333.6038.77.DC1.html>

A list of selected additional articles on the Science Web sites **related to this article** can be found at:

<http://www.sciencemag.org/content/333/6038/77.full.html#related>

This article appears in the following **subject collections**:

Atmospheric Science

<http://www.sciencemag.org/cgi/collection/atmos>